Ionics
https://doi.org/10.1007/s11581-025-06193-5

RESEARCH

Design and fabrication of *Punica granatum* peel-derived NSCQD/iron hexacyanoferrate ternary composite for simultaneous detection of ascorbic acid, uric acid, and resorcinol

D. Sivagurunathan[1] · Simon Deepa[2] · M. Devendiran[3] · R. A. Kalaivani[1]

Received: 24 December 2024 / Revised: 14 February 2025 / Accepted: 3 March 2025

Abstract
This work reports the synthesis of a novel paraffin-impregnated graphite electrode (PIGE) modified by N- and S-doped carbon quantum dot (NSCQD)/iron hexacyanoferrate composite for the electrochemical detection of resorcinol (RS), uric acid (UA), and ascorbic acid (AA). Using pomegranate (*Punica granatum*) peel as the carbon source, the NSCQDs were synthesized in an environmentally friendly manner. When combined with FeHCF, the NSCQDs formed a high-performance composite with enhanced electrochemical properties. The morphology, crystallinity, and chemical composition of the composite were investigated by X-ray diffraction (XRD), field emission scanning electron microscopy (FESEM), and X-ray photoelectron spectroscopy (XPS) analysis, respectively, which revealed a structure that was clearly defined and contained active spots that were suitable for redox reactions. Electrochemical tests revealed the sensor's high sensitivity, measuring 523.4 mA/mol/L for AA, 451.22 mA/mol/L for UA, and 372.1 mA/mol/L for RS. The sensor has low limits of detection of 2×10^{-6} mol/L, 3×10^{-6} mol/L, and 5×10^{-6} mol/L for AA, UA, and RS, respectively, with a linear detection range of 10×10^{-6} mol/L to 8000×10^{-6} mol/L for all analytes. Superior conductivity was brought about by the addition of graphene, redox activity was increased by FeHCF, and enhanced adsorption and catalysis were achieved by the introduction of electron-rich sites by NSCQDs. The identification of AA in Limcee tablets, UA in Allopurinol tablets, and RS in hair color solutions served as examples of real-world applicability. The electrode outperformed traditional electrodes in terms of sensitivity and decreased oxidation potential, and it demonstrated outstanding stability, maintaining 95% of its performance after 50 cycles. This study demonstrates the NSC/FeHCF-modified PIGE's potential for real-world uses in environmental monitoring, pharmaceutical quality assurance, and clinical diagnostics.

Keywords *Punica granatum* peel · NSCQD · NSCQD/FeHCF hybrid electrode · AA, UA, and RS detection

Introduction

Ascorbic acid (AA), also known as Vitamin C, is an important nutrient that belongs to the acidic hexose derivative family and is predominantly obtained from fresh fruits and vegetables. It is important for human health because it acts as a potent antioxidant, lowering the risk of chronic diseases such as cancer. Inadequate amounts of AA in the human body can result in scurvy, a condition marked by symptoms such as anemia, gum disease, and decreased immunity [1, 2]. Uric acid (UA), which is the end product of purine metabolism, leaves the body through urine, feces, and sweat. To avoid metabolic problems like gouty nephropathy, gout pain, hyperuricemia, and anemia, it is important to keep the UA level at a healthy level [3, 4]. Resorcinol (RS), a phenolic chemical that is used in many consumer goods like drugs, cosmetics, and glue, is very harmful to the environment and stays in the environment for a long time. Long-term exposure to RS can hurt people's health and the health of environments [5, 6]. The simultaneous detection of AA, UA, and RS is essential for clinical diagnosis, environmental monitoring,

✉ R. A. Kalaivani
director.sbs@velsuniv.ac.in

[1] Centre for Energy and Alternative Fuels, Department of Chemistry, School of Basic Sciences, Vels University, Pallavaram, Chennai, Tamil Nadu 600117, India

[2] Department of Chemistry, Vels Institute of Science and Technology and Advanced Studies, Pallavaram, Chennai, Tamil Nadu 600117, India

[3] Central Instrumentation Laboratory, Vels University, Pallavaram, Chennai, Tamil Nadu 600117, India

Published online: 22 March 2025

and industrial quality control because of their physiological and environmental significance. The permissible limits of these analytes are subject to change depending on the specific application. The recommended daily intake of AA is 65–90 mg, with an upper limit of 2000 mg per day, as per FDA guidelines. The normal serum concentration of UA in males is 3.4–7.0 mg/dL, while in females it is 2.4–6.0 mg/dL. Hyperuricemia is indicated by levels exceeding 7.0 mg/dL (WHO). In cosmetics, the maximum permissible concentration of RS is 0.5% (5 mg/mL) in accordance with EU regulations. In wastewater, the admissible limit is 0.1 mg/L (100 µg/L) as per the US EPA. RS is regulated in a variety of industries. The electrochemical sensor that has been proposed has the ability to detect these analytes at levels that are significantly lower than their critical thresholds. Consequently, it is highly relevant for environmental, pharmaceutical, and biomedical applications. However, detecting these compounds simultaneously presents significant challenges due to their identical oxidation potentials. These analytes result in low selectivity and sensitivity because they create overlapping anodic peaks on common bare electrodes, like glassy carbon electrodes (GCEs). Furthermore, efficient detection is hampered by electrode fouling brought on by the adsorption of chemical byproducts. Because of these challenges, better electrode materials that can differentiate between the redox behavior of AA, UA, and RS while offering higher sensitivity and selectivity are required. Although conventional analytical techniques including spectrophotometry and chromatography yield reliable findings, they have disadvantages including high costs, time consumption, and intricate instrumentation requirements [7]. Electrochemical sensing has emerged as a viable option owing to its user-friendliness, rapid response time, affordability, and high sensitivity. The electrochemical detection of AA, UA, and RS relies on their inherent redox activity, facilitating measurement using electrochemical signals [8–10].

In recent years, nanostructured materials have been extensively studied for the development of electrochemical sensors capable of detecting AA, UA, and other biologically relevant compounds such as dopamine (DA) and RS [11]. Metal hexacyanoferrate (MHCF) composites have received special attention due to their superior redox characteristics, electron-mediating capacity, and structural plasticity. These properties make MHCF-based composites very successful at increasing sensor sensitivity and selectivity [12, 13]. Furthermore, their capacity to build stable coordination frameworks with varied metal centers allows for fine-tuning of electrochemical behavior, which is critical for the accurate and simultaneous detection of multiple analytes. Several transition metal hexacyanoferrates (TMHCFs) have received attention for their potential use in sensing technologies due to their unique redox characteristics and structural flexibility. Nickel hexacyanoferrate (NiHCF) is a popular choice for dopamine sensors due to its steady redox behavior and high catalytic efficiency [14]. CuHCF has demonstrated remarkable performance in heavy metal detection due to its strong electron-mediating capabilities [15]. Similarly, zinc hexacyanoferrate (ZnHCF) has been used in electrochemical sensing for environmental monitoring, but manganese hexacyanoferrate (MnHCF) is used due to its better electrocatalytic activity in detecting biologically important compounds [16, 17]. Among these, iron hexacyanoferrate (FeHCF) stands out for its exceptional redox characteristics, electron transport capabilities, and environmental sustainability. FeHCF has Fe (II)/Fe (III) redox centers, which enable efficient electron mediation in electrochemical reactions [18, 19]. The addition of MHCF to advanced nanocomposites, such as those containing graphene or doped carbon materials, improves electron transport, stability, and overall sensor performance, making them essential in the field of current electrochemical sensing.

Carbon dots (C-Dots), a type of zero-dimensional nanomaterial, have received a lot of attention due to their unusual capabilities, which include great photoluminescence, high biocompatibility, tunable optical features, strong chemical stability, and exceptional electrical conductivity [20]. These properties make C-Dots ideal for the development of electrochemical and optical sensors that can detect a wide range of analytes, including biomolecules, environmental contaminants, and dangerous chemicals [21, 22]. Their small size and high surface-to-volume ratio promote electron transit, increasing sensitivity and allowing for exact quantification in sensing devices. Furthermore, their low toxicity, ease of synthesis, and cost-effectiveness make C-Dots an excellent candidate for sophisticated sensing applications. Heteroatom doping has been intensively studied to increase the performance of C-Dots. Nitrogen and S co-doped carbon dots (NSCQDs) have received a lot of attention because of their synergistic properties. Nitrogen doping enhances electron density, while S doping adds electron-donating characteristics, which improves charge transfer, redox activity, and catalytic performance [23]. NSCQDs provide greater sensitivity and selectivity in sensing applications, as well as reduced photoluminescence quenching, resulting in lower detection limits and improved performance in real-world circumstances [24]. CQDs can be synthesized using a variety of methods including hydrothermal/solvothermal synthesis [25, 26], microwave-assisted synthesis [27], and pyrolysis [28], which rely on the carbonization of organic precursors. Among these approaches, green synthesis has gained popularity due to its environmental friendliness, cost-effectiveness, and sustainability. Green synthesis uses renewable and biodegradable biomass waste to produce highly functioning CQDs without the use of toxic chemicals. In this study, we used a green synthesis technique to create CQDs from *Punica granatum* (pomegranate) peel, a commonly available

and renewable biomass waste. The generated NSCQDs were combined with a graphene and iron hexacyanoferrate (FeHCF) matrix to form a high-performance ternary composite. Graphene, with its superior conductivity, huge surface area, and mechanical durability, provides a strong platform for the composite, while FeHCF contributes good redox characteristics and selectivity to target analytes. The incorporation of NSCQDs into this hybrid matrix increases the composite's electrochemical activity, allowing for the simultaneous detection of physiologically and ecologically relevant analytes. This study demonstrates the potential of biomass-derived NSCQDs for developing sustainable and high-performance sensing devices.

This study aims to enhance the efficiency and feasibility of the simultaneous detection of AA, UA, and RS by synthesizing a single NSCQD/FeHCF-modified PIGE electrode. These analytes often coexist in biological, pharmacological, and environmental samples; nevertheless, their overlapping oxidation potentials pose a significant obstacle to selection. The composite electrode efficiently addresses this issue by facilitating distinctly separated oxidation peaks, hence providing precise detection. Utilizing the redox-active FeHCF, highly conductive graphene, and electron-rich NSCQDs, the sensor demonstrates superior electrocatalytic activity, better charge transfer, and improved detection thresholds. An extensive electrochemical assessment was performed utilizing both cyclic voltammetry (CV) to examine redox behavior and differential pulse voltammetry (DPV) for trace-level quantification, ensuring accurate and dependable sensing. This work is scientifically significant as it establishes a cost-efficient, single-step platform for multi-analyte detection, hence minimizing material usage, analysis duration, and apparatus intricacy. This dual-strategy method improves sensitivity, reproducibility, and selectivity, rendering the sensor a valuable instrument for environmental, pharmaceutical, and therapeutic applications, fulfilling a significant demand in electrochemical sensing technology.

Experimental procedure

Materials

The composites were prepared using analytical reagent-grade chemicals, such as iron (III) chloride hexahydrate ($FeCl_3 \cdot 6H_2O$) (99%), potassium hexacyanoferrate (III) ($K_3[Fe(CN)_6]$) (99%), thiourea (99%), graphene, sodium hydroxide, hydrochloric acid, and ethanol. All chemicals were obtained from SRL Laboratories in Chennai, India. Paraffin Impregnated Graphite Electrode (PIGE) was received from M/S Piramal Enterprises, Chennai. Merck India Ltd. supplied the key acids, bases, and solvents needed in this study. All compounds were utilized as obtained, without further purification.

Synthesis of N, S co-doped carbon quantum dot from *Punica granatum* peels

N and S co-doped carbon quantum dots (NSCQDs) were synthesized using *Punica granatum* peel as a carbon source and thiourea for N and S doping. Due to its high carbon content, natural precursors, and superior electrochemical properties, pomegranate peel was selected over other biomass waste materials. Polyphenols, flavonoids, and amino acids enhance the production of heteroatom-doped CQDs without the need for chemical doping. Furthermore, its widespread availability as a bio-waste material makes it an economically viable and environmentally sustainable choice. Fresh pomegranate peels were collected, thoroughly washed with distilled water, and dried in an oven at 60 °C for 24 h. The dried peels were ground into a fine powder with a mechanical grinder. One gram of pomegranate peel powder was dispersed in 50 mL of distilled water in a Teflon-lined stainless steel autoclave, and 0.5 g of thiourea was used as a doping agent. The mixture was rapidly agitated for 30 min to establish homogeneity and then sealed and heated at 180 °C for 8 h. After naturally cooling to room temperature, the reaction liquid was filtered to eliminate any unprocessed particles and impurities. The filtrate was centrifuged at 10,000 rpm for 15 min to remove bigger particles and contaminants. To remove excess ions and small molecules, the supernatant containing NSCQDs was filtered through a dialysis membrane (molecular weight cutoff ~ 1 kDa) against distilled water for 24 h. The purified NSCQDs were then stored for characterization and usage in composite construction after being vacuum-dried at a temperature of 50 °C.

Synthesis of iron hexacyanoferrate (FeHCF) and NSCQD/FeHCF

Iron hexacyanoferrate was synthesized by preparing two separate solutions: one containing 0.1 M $FeCl_3 \cdot 6H_2O$ dissolved in deionized water and another containing 0.1 M $K_3[Fe(CN)_6]$ dissolved in deionized water. The solutions were mixed and agitated for 2–3 h, resulting in FeHCF precipitation from the direct interaction between Fe^{3+} and $[Fe(CN)_6]^{3-}$ ions. The reaction mixture was matured at room temperature for 24 h to increase crystallinity and particle uniformity. The resultant precipitate was centrifuged, extensively washed with deionized water to remove unreacted precursors, and then dried at 60 °C for 12 h to yield FeHCF powder. To synthesize the NSCQD/FeHCF composite, as prepared FeHCF was dissolved in deionized water and ultrasonically dispersed for 1 h for uniform dispersion. The produced NSCQDs were then added to it in the ratio of 10:1

and ultrasonically mixed for 1 h to achieve a homogenous mixture. The dispersion was transferred to a Teflon-lined stainless-steel autoclave and heated to 120 °C for 6 h. After cooling to ambient temperature, the composite was washed with deionized water and ethanol to remove contaminants and then dried in a vacuum oven at 60 °C for 12 h. The resultant sample was labeled as NSCQD/FeHCF.

Fabrication of NSCQD/FeHCF electrode

The NSCQD/FeHCF composite was synthesized as described above. For electrode fabrication, 2 mL of graphene dispersion was added to enhance conductivity. The prepared NSCQD/FeHCF composite was dispersed in ethanol and ultrasonicated for 30 min to obtain a homogeneous suspension. A 10 mL of (0.1 mol/L) aliquot of this suspension was drop-cast onto the polished PIGE surface to ensure complete coverage. The electrode was then air-dried at ambient temperature, followed by vacuum drying at 60 °C for 2 h to enhance stability. The resulting NSCQD/FeHCF-modified PIGE with graphene was then used for electrochemical analysis of AA, UA, and RS. The scheme of the overall process is depicted in Fig. 1.

Characterization

X-ray diffraction (XRD) investigation with a Rigaku D/MAX 2500 V system furnished with Cu Kα radiation ($\lambda = 1.5406$ Å) validated the crystal structures of the films. To analyze the optical properties of samples, diffuse reflectance and absorbance spectra were evaluated with a UV–VIS-NIR Perkin Elmer spectrophotometer. Fourier transform infrared (FTIR) spectroscopy was performed using a VERTEX 80v equipped with a HYPERION 2000 microscope (Bruker Optics, Germany). High-resolution scanning electron microscopy (HRSEM) on an FEI Quanta FEG 200 system using an accelerating voltage of 20 kV was used to investigate the morphology of the electrochemically produced samples. Energy-dispersive X-ray spectroscopy (EDS) coupled with the HRSEM configuration revealed elemental composition. An X-ray photoelectron spectrum (ESCA 3100, Shimadzu) measured elemental analysis of as-synthesized materials. Electrochemical studies were carried out using an Eco Chemie Autolab Potentiostat device under computational control. A standard three-electrode setup was employed, consisting of the prepared NSCQD-FeHCF composite as the working electrode, a platinum wire as the auxiliary electrode, and an Ag/AgCl electrode (saturated in 0.1 M KCl) as the reference electrode. KCl was chosen over PBS as the supporting electrolyte due to its high ionic conductivity, minimal electrochemical interference, and compatibility with FeHCF-based electrochemical systems, ensuring stable and reproducible redox responses.

Results and discussion

Crystalline phase analysis

The XRD analysis was employed to investigate the structural and crystalline properties of the synthesized samples, as illustrated in Fig. 2, which displays the XRD pattern of the samples. As shown in the figure, the XRD pattern of NSCQD demonstrates unique structural characteristics, including a broad peak centered at 23.2° that suggests the presence of amorphous carbon or partially disordered graphitic layers [29]. The interlayer spacing of graphitic carbon materials is characterized by a broad peak that is representative of the (002) plane [30]. This peak is larger than that of well-ordered graphite as a result of doping-induced lattice distortions. Furthermore, the structure is suggested to contain localized graphitic domains, as evidenced by the presence of two small but sharp peaks at 25.3° and 26.8°, which correspond to graphitic crystalline regions. These peaks may be the result of N and S doping, which increases the graphitic nature by introducing defects and crystallinity in specific regions [31]. The combined nature of NSCQD,

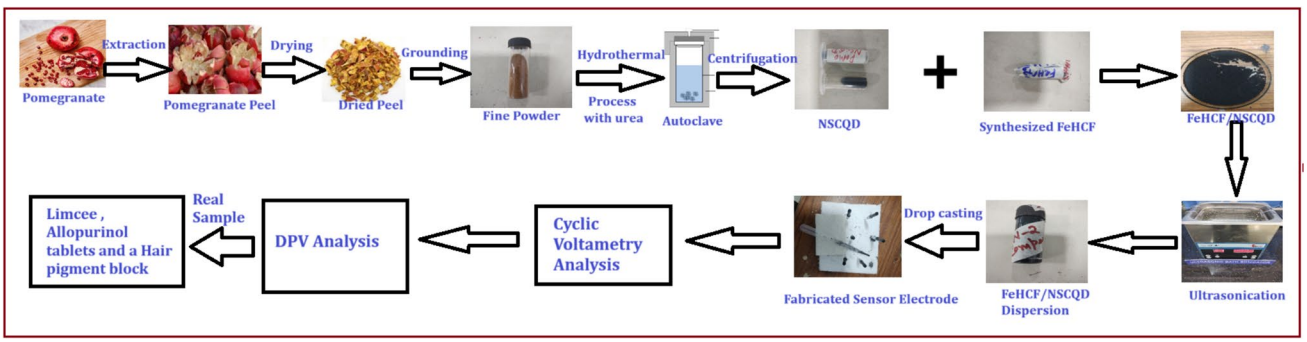

Fig. 1 Schematic illustration of the fabrication of NSCQD/FeHCF composite for AA, UA, and RS detection

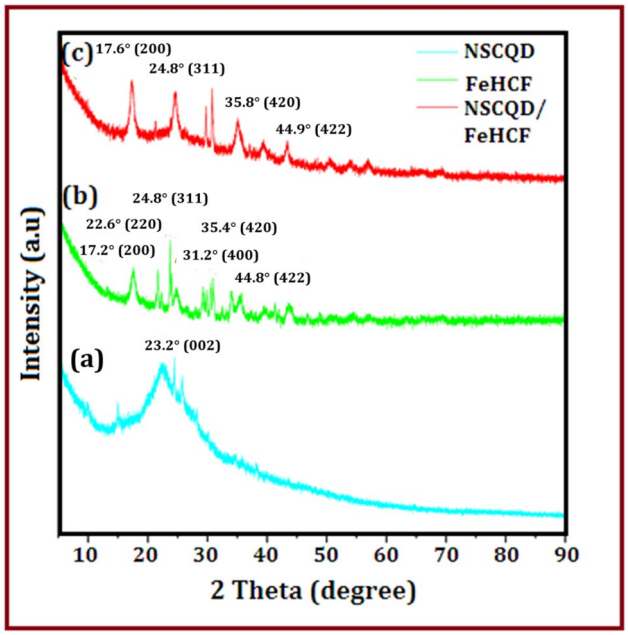

Fig. 2 Powder XRD patterns of (**a**) NSCQD, **b** FeHCF, and (**c**) NSCQD/FeHCF

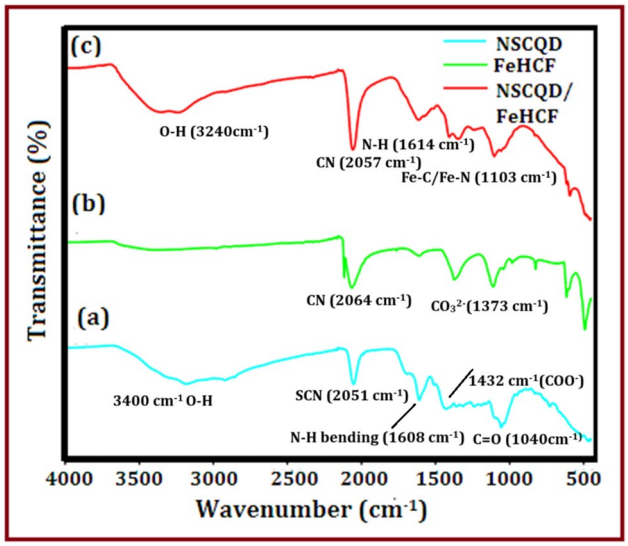

Fig. 3 FTIR spectra of (**a**) NSCQD, **b** FeHCF, and (**c**) NSCQD/FeHCF

which is characterized by the coexistence of amorphous and crystalline features, is reflected in the combination of the broad peak and sharp peaks, which contribute to its distinctive electrochemical properties. This structural synergy enables the development of active surface sites and improved conductivity for sensing applications [32]. The diffraction peaks of FeHCF closely correspond with those of the standard sample (PDF#00–73–0687), affirming that the material possesses a cubic face-centered structure [33]. The principal diffraction peaks occur at roughly 17.2°, 22.6°, 24.8°, 31.2°, 35.4°, and 44.8°, aligning with the (200), (220), (311), (400), (420), and (422) crystallographic planes, respectively. The XRD pattern of the NSCQD/FeHCF composite demonstrates notable structural alterations relative to the individual components. Significantly, multiple peaks within the range of 20°–30° 2θ are missing, and a peak at 26.7° 2θ is not detected, signifying the amorphous characteristics of the carbon in the composite. A pronounced peak at 24.8° 2θ, associated with the (311) crystal plane of FeHCF, indicates improved crystallinity resulting from the interaction between NSCQD and FeHCF, underscoring the synergistic structural integration within the composite. The Debye–Scherrer formula was employed to determine the crystallite size of the synthesized samples [34]. The abrupt peak at 24.8° 2θ, which corresponds to the (311) plane of FeHCF, suggests an estimated crystallite size of approximately 51 ± 3 nm.

FTIR analysis

The presence of different functional groups in the synthesized samples is confirmed by the FTIR spectrum shown in Fig. 3. The FTIR spectrum of NSCQD displays key peaks at 3180 cm^{-1}, corresponding to OH stretching vibrations, 1608 cm^{-1} for NH_2 bending vibrations, 1432 cm^{-1} for COO^{-1} stretching vibrations, and 1040 cm^{-1} for C = O stretching vibrations [35]. Additionally, a prominent peak at 2051 cm^{-1} suggests the presence of the –SCN group in the compound. The pristine FeHCF displays distinct peaks in its infrared spectrum. These peaks are observed at 2116 cm^{-1} and 2064 cm^{-1} for cyanide (C≡N) stretching, 1373 cm^{-1} for symmetric stretching of CO_3^{2-}, 1110 cm^{-1} for Fe–C bonds, and 614 cm^{-1} and 491 cm^{-1} for Fe–N stretching [36]. Additionally, a broad peak is present in the range of 3300–3400 cm^{-1} corresponding to O–H stretching. The successful integration of NSCQD and FeHCF is confirmed by the peaks observed in the FTIR spectrum of the composite, which are located at 3245 cm^{-1}, 2057 cm^{-1}, 1614 cm^{-1}, 1345 cm^{-1}, 1103 cm^{-1}, and 593 cm^{-1}. The presence of O–H stretching is suggested by the prominent peak observed at 3245 cm^{-1}, whereas the preservation of the C≡N group is confirmed by the peak at 2057 cm^{-1}. The peaks observed at 1614 cm^{-1} and 1345 cm^{-1} are associated with NH_2 and COO^{-1} groups, while those at 1103 cm^{-1} and 593 cm^{-1} are assigned to Fe–C and Fe–N stretching, respectively [37]. These findings confirm the structural stability of the composite.

Morphological analysis

The SEM image (Fig. 4a) reveals the morphological structure of NSCQDs, showing a well-dispersed and uniform nanoscale distribution. The elemental mapping images (Fig. 4b, c) confirm the successful incorporation of nitrogen (N) and sulfur (S) into the CQD framework, with a homogeneous distribution across the observed region. In addition to this, EDAX spectra depicted in Fig. 4d confirm the presence of N and S on the carbon framework. This suggests that the doping process was effective, enhancing the potential electrochemical properties of NSCQDs. Figure 5a, b depicts the FESEM images of the NSCQD/FeHCF composite, which were obtained at 2 µm and 200 nm magnifications and exhibit a hybrid morphology that is defined by the integration of NSCQD onto the FeHCF framework. The composite exhibits a relatively uniform distribution of aggregated particles at low magnification, which suggests that the material exhibits good homogeneity and structural integrity. The nanoscale features of the composite are emphasized in high-magnification images, which depict NSCQD as finely dispersed particles or coatings on the granular FeHCF surface. The surface complexity is enhanced by the intimate interaction between NSCQD and FeHCF, as no significant fractures or voids are observed. The composite's surface area and active sites are significantly increased by this hybrid morphology, rendering it well-suited for advanced applications. The EDS layered analysis (Fig. 5c) demonstrates that essential elements are distributed uniformly, maintaining composite homogeneity. The elemental mapping (Fig. 5d) demonstrates the even integration of NSCQD while preserving the FeHCF framework. Finally, the EDAX spectrum (Fig. 5e) confirms the presence of all predicted elements, indicating the material's purity and stoichiometric composition. These findings support the effective synthesis of the NSCQD/FeHCF composite, which has a well-defined structure. The TEM image (Fig. 6a, b) depicts the nanoscale morphology of the NSCQD/FeHCF composite, revealing a

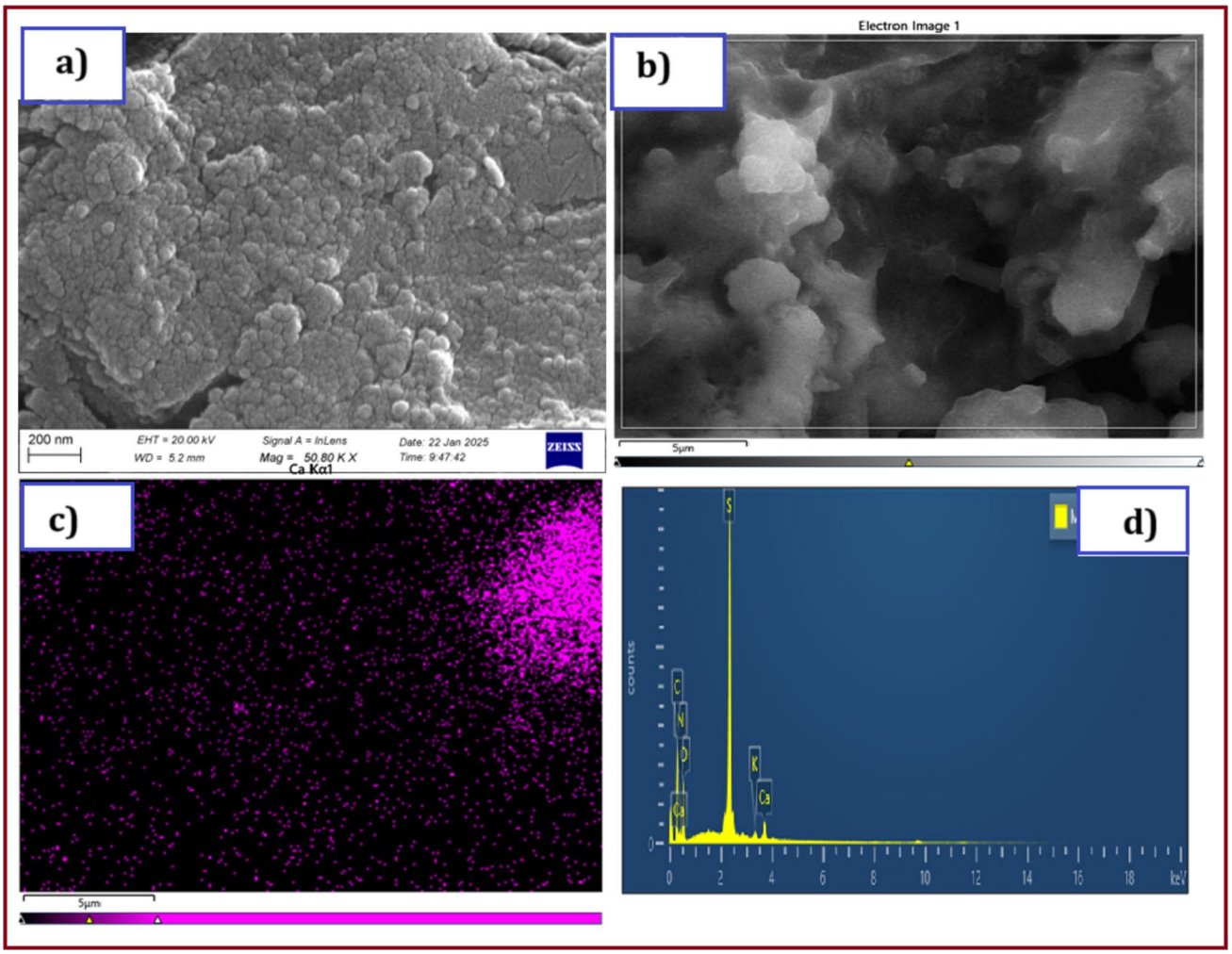

Fig. 4 **a** FESEM image of NSCQD (**b**) and **c** elemental mapping images of NSCQD; **d** EDAX spectra of NSCQD

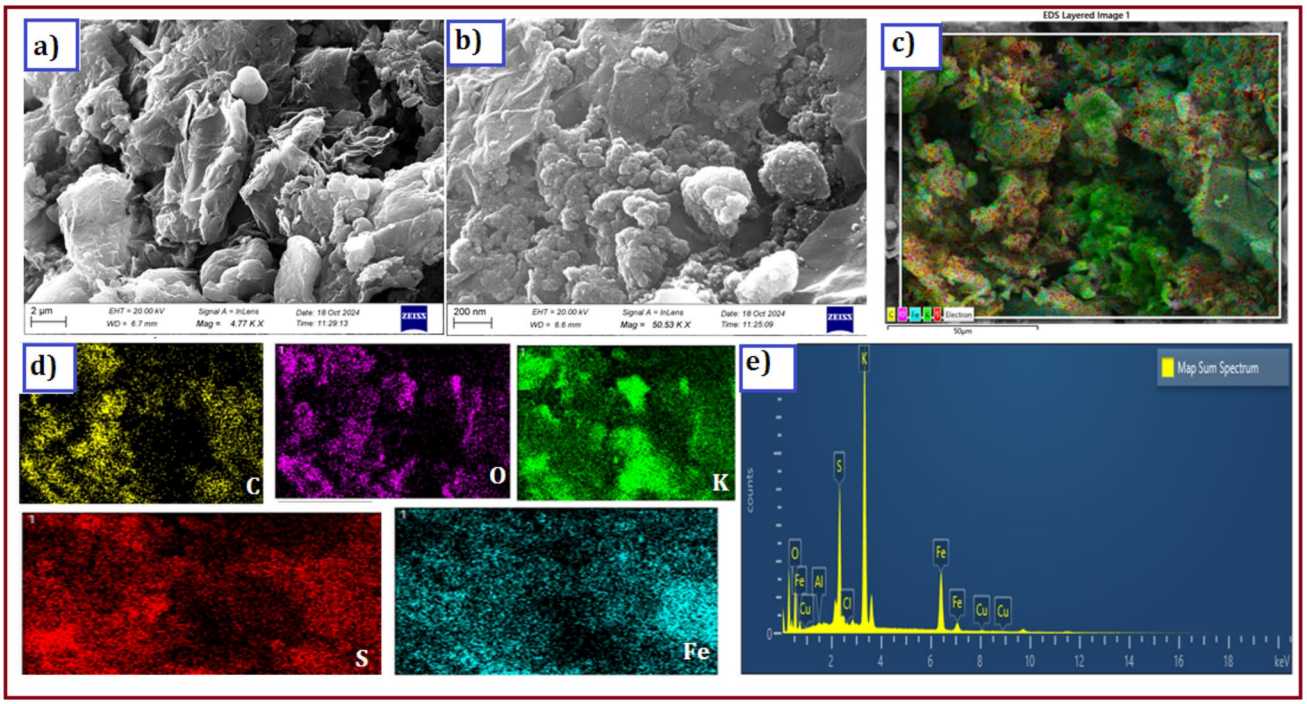

Fig. 5 **a**, **b** FESEM images of NSCQD/FeHCF at 2 µm and 200 nm, respectively; **c** EDS layered analysis image; **d** elemental mapping images; **e** EDAX spectra of NSCQD/FeHCF

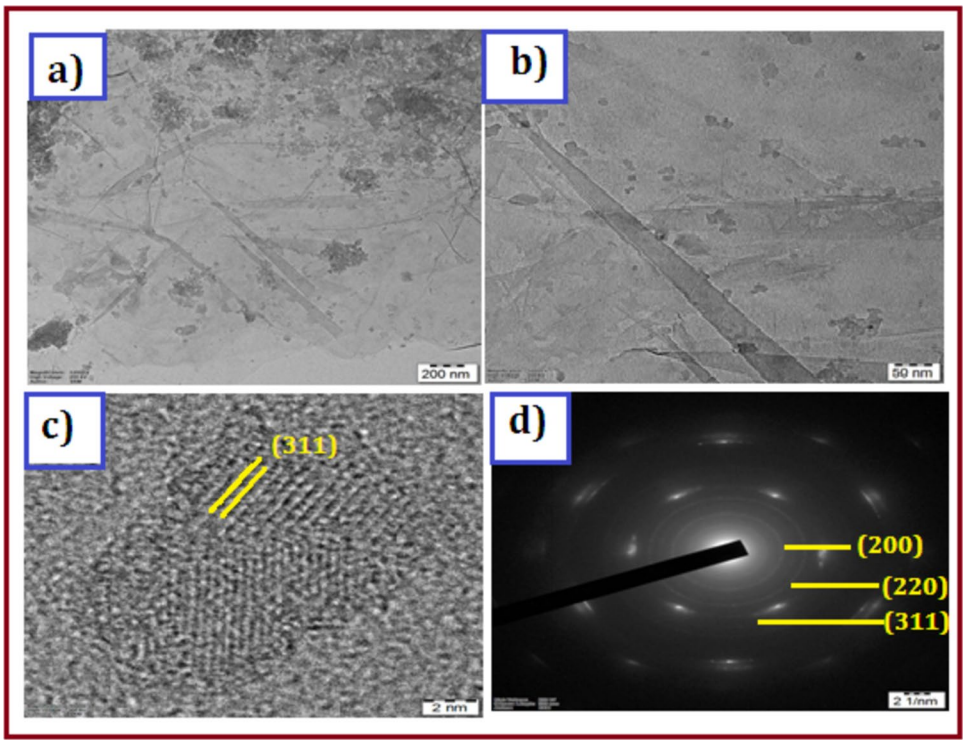

Fig. 6 **a**, **b** TEM images of NSCQD/FeHCF; **c** HRTEM image of NSCQD/FeHCF; **d** SAED pattern of NSCQD/FeHCF

homogeneous distribution of NSCQD particles across the FeHCF matrix. The HRTEM image (Fig. 6c) shows well-defined lattice fringes corresponding to the (311) plane of FeHCF, coupled with amorphous patches attributable to NSCQD, confirming the composite's hybrid structure and strong interface. The SAED pattern (Fig. 6d) supports

the crystalline structure of FeHCF, with diffraction rings indexed to the (200), (220), and (311) planes, as well as the amorphous contribution from NSCQD. These findings support the effective synthesis and structural integrity of the NSCQD/FeHCF composite.

Chemical composition and surface state analysis

The chemical states and elemental composition of the samples were examined using XPS analysis to investigate their chemical characteristics and interactions. The survey scan spectrum depicted in Fig. 7a shows Fe, C, N, S, and O components in the NSCQD/FeHCF composite, confirming successful integration. Strong signals from Fe and N indicate the structural integrity of the FeHCF framework, whereas S and C confirm NSCQDs' participation. Composite phase purity is confirmed by the absence of unexpected peaks. The high-resolution Fe 2p spectra depicted in Fig. 7b show two peaks at 711.0 eV (Fe $2p_{3/2}$) and 724.5 eV (Fe $2p_{1/2}$), indicating the Fe^{3+} oxidation state in the FeHCF lattice [38]. In addition, the presence of satellite peaks supports iron oxidation and chemical stability in the composite structure. As shown in Fig. 7c, the deconvoluted C 1 s spectrum displays peaks around 284.6 eV (C–C/C = C), 286.0 eV (C–O), and 288.5 eV (C = O), indicating the presence of graphitic and oxygenated carbon species from NSCQDs [39]. The characteristic sp^2 hybridized carbon peak confirms the conductive nature of the composite, which is beneficial for electrochemical applications. The N 1 s spectra show peaks at 398.5 eV (Fe–N≡C) and 400.1 eV (graphitic-N), indicating nitrogen-coordinated Fe centers from FeHCF and nitrogen doping from NSCQDs. NSCQDs and FeHCF interact strongly, which may improve electron transport [40] (Fig. 7d). The S 2p spectra show peaks at 163.8 eV (S $2p_{3/2}$) and 165.1 eV (S $2p_{1/2}$), suggesting sulfur in the NSCQD-derived thiol or thiophene-like structure (Fig. 7e) [41]. The XPS results collectively confirm the successful formation of the NSCQD/FeHCF composite with proper elemental incorporation. The strong interaction between NSCQDs and FeHCF enhances electron transfer efficiency, making the composite highly suitable for electrochemical applications.

CV analysis for detection of AA, UA, and RS by NSC/Gr/FeHCF-modified PIGE

The electrochemical oxidation efficacy of AA was assessed using the NSCQD/FeHCF-modified PIGE through CV measurements in 0.1 M KCl electrolyte (pH 7.0). The potential window ranged from − 1.0 V to + 1.0 V, with a scan rate of 50 mV/s. The electrode was subjected to 50 continuous cycles to evaluate its stability and reproducibility. The oxidation peak for AA, which was recorded in KCl containing 0.002 mol/L AA, was located at 0.521 V on the unmodified PIGE. In the absence of AA, no peak was observed for the NSC/Gr/FeHCF-modified PIGE in KCl as a control experiment, thereby confirming the electrode's inactivity in

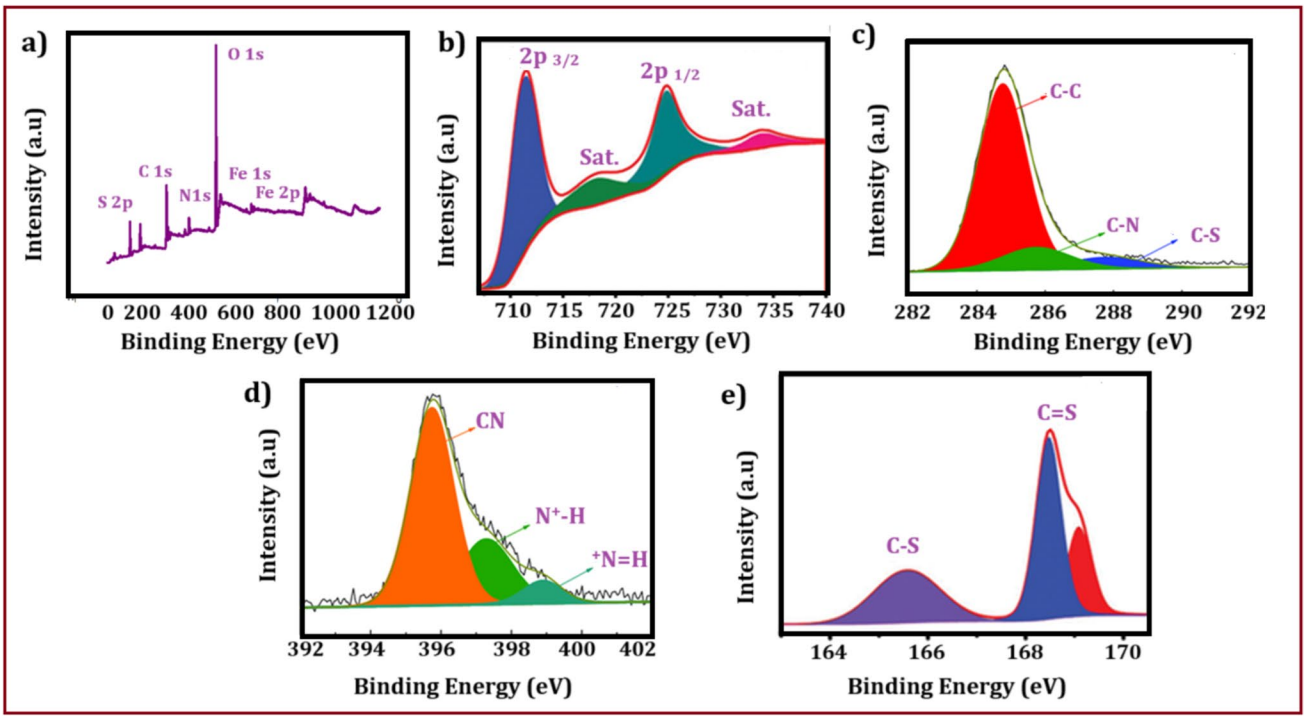

Fig. 7 XPS spectra. **a** Survey scan spectra of NSCQD/FeHCF; high-resolution spectra of **b** Fe 2p, **c** C 1 s, **d** N 1 s, and **e** S 2p

the absence of the analyte. On the other hand, an oxidation peak for AA was substantially augmented at 0.192 V over the NSC/Gr/FeHCF-modified PIGE at a scan rate of 50 mV/s (Fig. 8a). The CV spectra show two separate sets of redox peaks, particularly, first oxidation peak at ~ 0.6 V with a corresponding reduction peak at ~ 0.55 V and a second oxidation peak at ~ 0.1 V with a reduction peak at ~ 0.0 V. The redox pair at ~ 0.6 V and ~ 0.55 V is due to the Fe (II)/Fe (III) transition in FeHCF, which enhances the electron transport mechanism. Meanwhile, the redox peaks at 0.1 V and 0.0 V are mostly due to electron-rich locations in NSC-QDs and graphene, which allow for efficient charge transport and analyte interactions. The oxidation peak at ~ 0.6 V is used for calibration curve fitting because of its great current response, sensitivity, and linearity in electrochemical detection. The FeHCF-mediated electron transfer at this potential enables effective analyte oxidation, resulting in better sensor performance and reproducibility. The modified electrode's superior catalytic activity was evident in the peak current, which increased by approximately 20-fold in comparison to the unmodified PIGE. This enhancement is due to the NSC/FeHCF composite's synergistic effect between its components, which enables a faster diffusion and an enhanced electron transfer rate [42]. The NSC//FeHCF-modified PIGE's superior efficacy in the electrochemical detection of AA is underscored by the substantial increase in peak current and the reduced oxidation potential. The conductive nature of graphene, the high redox activity of FeHCF, and the synergistic integration of nitrogen and sulfur functionalities in the composite are likely the reasons for the enhanced electrocatalytic activity, as demonstrated by these results [43]. In addition, the concentration of AA ranged from 10×10^{-6} to 10^{-6} mol/L, and the associated CV profiles demonstrated a gradual increase in oxidation peak current with rising AA concentration. The linear correlation between peak current and AA concentration underscores the heightened sensitivity and extensive detection range of the NSC/FeHCF-modified PIGE, rendering it appropriate for both trace-level detection and practical applications (Fig. 8b). The regression equations for the AA oxidation peak current (Ipa) and reduction peak current (Ipc) were determined as follows:

$$\text{Ipa} = 0.5234([\text{AA}]/\mu\text{M}) - 3.1245 (R^2 = 0.9963)$$
$$\text{Ipc} = -0.1746([\text{AA}]/\mu\text{M}) + 0.9023 (R^2 = 0.9971)$$

Here, the slope values (0.5234 for Ipa and − 0.1746 for Ipc) indicate the sensitivity of the electrode to AA concentration, while the high correlation coefficients ($R^2 > 0.99$) confirm excellent linearity. These equations further demonstrate the reliability of the NSC/FeHCF-modified PIGE for quantitative analysis of AA. The findings validate the electrode's exceptional electrocatalytic performance and effective electron transfer kinetics for AA oxidation. In addition, NSC/FeHCF-modified PIGE was used to identify UA and RS. Figure 9a, b shows CV profiles acquired at various concentrations of UA and RS with the NSCQD/FeHCF-modified PIGE, illustrating the sensor's electrochemical response and sensitivity to these analytes.

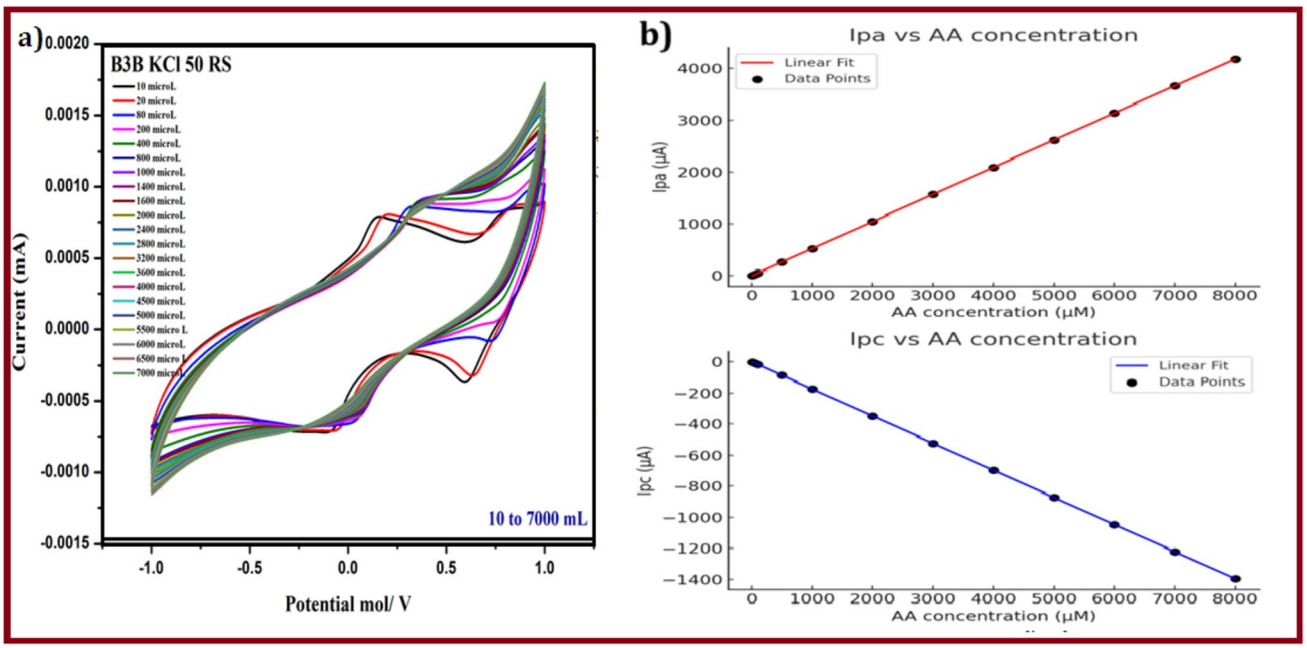

Fig. 8 **a** Cyclic voltammograms of AA detection at NSCQD/FeHCF-modified PIGE in 0.1 M KCl (pH 7.0) within a potential window of − 1.0 V to + 1.0 V at a scan rate of 50 mV/s and with 50 continuous cycles. **b** Linear relationship of Ipa and Ipc vs AA concentration

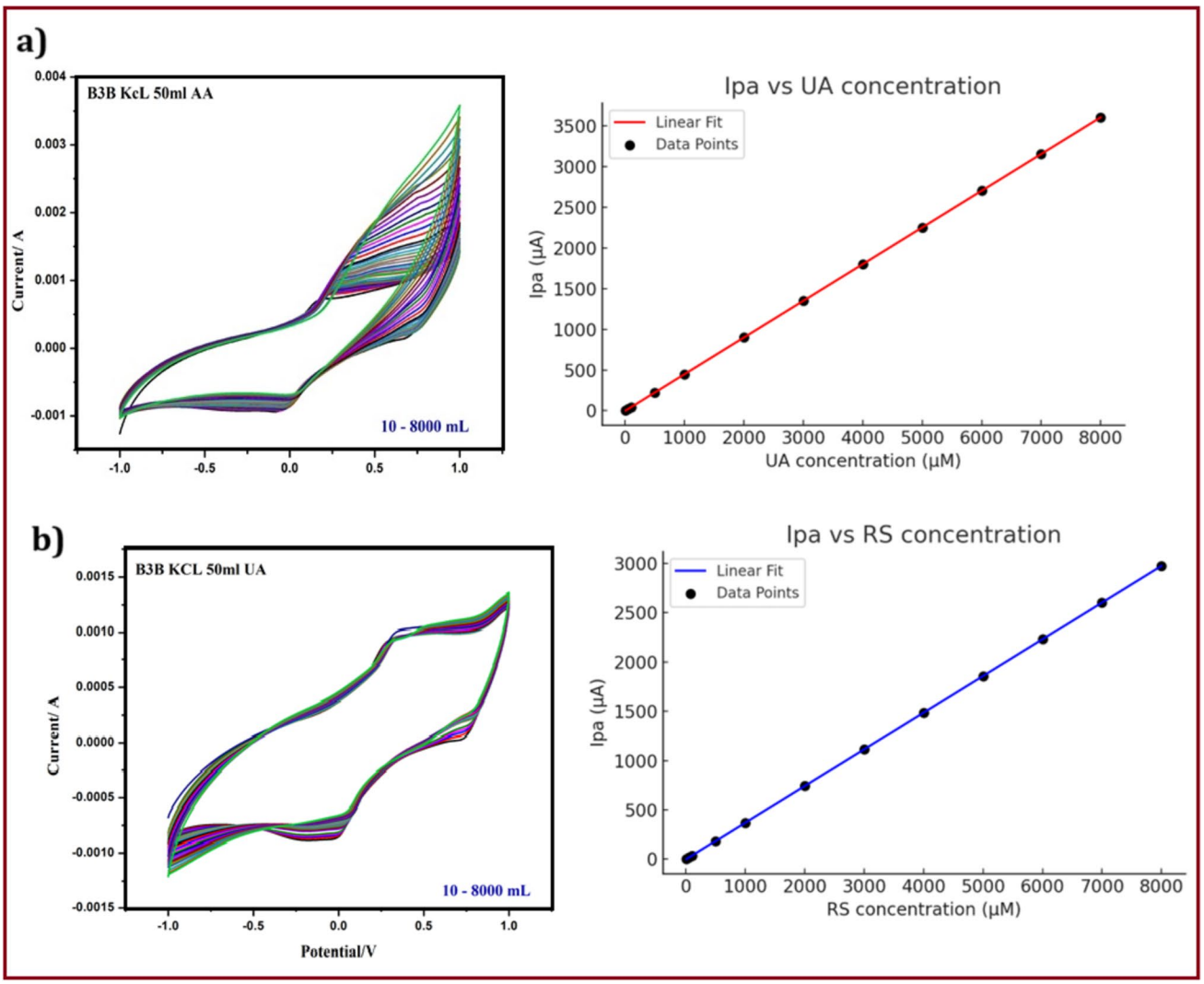

Fig. 9 **a**, **b** Cyclic voltammograms of UA and RS detection at NSCQD/FeHCF-modified PIGE in 0.1 M KCl (pH 7.0), with a potential window of − 1.0 V to + 1.0 V, using a scan rate of 50 mV/s and with 50 continuous cycles with a linear relationship of Ipa and Ipc vs UA, RS concentration

The CV profiles obtained for various UA concentrations (Fig. 9a) exhibited a well-defined oxidation peak at around 0.352 V, which moved and increased correspondingly with increasing UA concentration. The NSC/FeHCF-modified PIGE has a significantly lower oxidation potential than the untreated PIGE, indicating improved electrocatalytic activity. The improved reaction can be attributable to the synergistic interplay between the graphene matrix, which allows for quicker electron transmission, and the FeHCF component, which promotes efficient UA oxidation [44]. The oxidation peak current (Ipa) showed a strong linear connection with the concentration of UA, indicating the sensor's great sensitivity (Fig. 9b). The regression equation for UA oxidation was determined as follows: IPA (UA) = 0.4512([UA]/μM) − 2.6743 ($R^2 = 0.9958$). The slope value (0.4512) shows the electrode's great sensitivity to UA, and the high correlation coefficient ($R^2 = 0.9958$) supports the sensor's accuracy and reliability for UA quantification. These findings support the NSCQD/FeHCF-modified PIGE's superior performance in the selective and sensitive detection of UA in complicated samples. The NSCQD/FeHCF-modified PIGE was also evaluated for the detection of RS. The CV profiles exhibited a strong oxidation peak at around 0.457 V, with a progressive increase in peak current as the RS concentration increased. This improvement reflects the improved electrode's capacity to detect RS with high sensitivity but low detection potential. The interaction of RS with the active sites provided by FeHCF and the conductive graphene matrix leads to efficient electron transfer, which contributes to the electrode's outstanding performance [45]. The linear regression investigation of the oxidation peak current for RS resulted in the

following equation: Ipa (RS) = 0.3721 ([RS]/μM) – 1.9864 (R^2 = 0.9967). The slope value (0.3721) indicates the electrode's sensitivity to RS, and the high R^2 value (0.9967) reveals a good correlation between RS concentration and electrochemical response. This result demonstrates the electrode's good capability for quantitative detection of RS complex materials. The scan rate investigation for AA, UA, and RS was carried out independently utilizing the NSCQD/FeHCF-modified PIGE, and the associated CV profiles are shown in Fig. 10a–c. Each analyte was analyzed at different scan rates in a solution containing 50 mL of KCl and 1 mL of the analyte in question. The CV profiles for AA showed a significant rise in peak current ($_{Ipeak)}$ with increasing scan rate, showing a high dependence on the diffusion of AA molecules to the electrode surface, as shown in Fig. 10a. AA also had the greatest peak currents of the three analytes, indicating a robust interaction with the active sites of the NSCQD/FeHCF composite and improved electron transfer kinetics [46]. For UA, the CV profiles in Fig. 10b showed a linear connection between peak current and the square root of scan rate, suggesting a diffusion-controlled redox mechanism. UA's peak currents were moderate, lower than those of AA but higher than those of RS, indicating an effective but less noticeable interaction with the electrode as compared to AA. For RS, the CV profiles illustrated in Fig. 10c had the lowest peak currents, indicating diffusion-controlled behavior based on the linear connection between peak current and scan rate. These findings demonstrated the electrode's capacity to detect all three analytes efficiently while also emphasizing its higher catalytic activity for AA and UA oxidation.

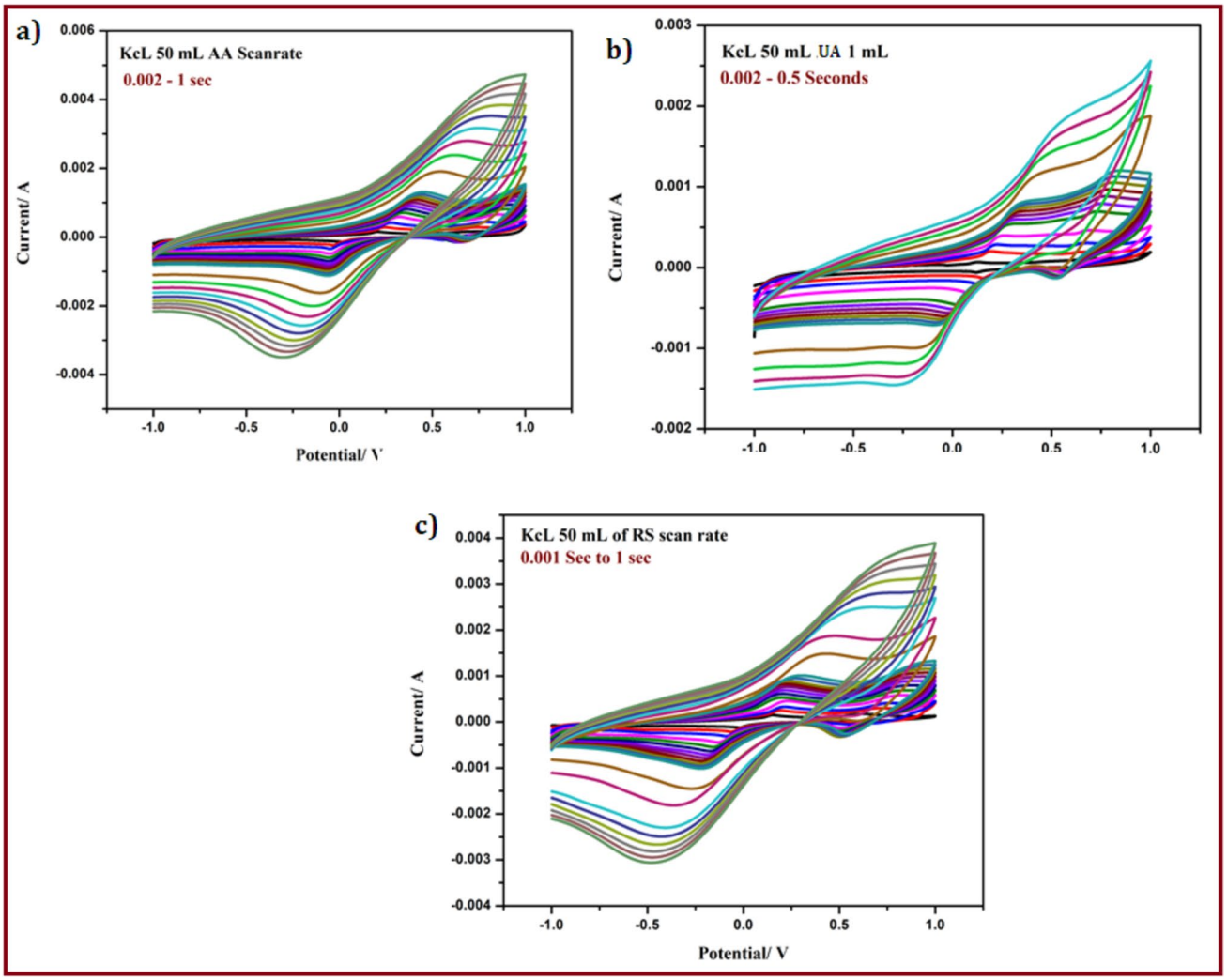

Fig. 10 Cyclic voltammetry profiles of the NSCQD/Gr/FeHCF-modified PIGE for **a** ascorbic acid, **b** uric acid, and **c** resorcinol recorded at varying scan rates

DPV analysis for detection of AA, UA, and RS by NSCQD//FeHCF-modified PIGE

The NSCQD/FeHCF-modified PIGE was used to perform DPV analyses for the detection of AA, UA, and RS in 0.1 M KCl electrolyte (pH 7.0). The applied potential window was − 1.0 V to + 1.0 V, with a pulse width of 50 ms, pulse height of 50 mV, and step time of 0.5 s to ensure accurate peak current measurements. As demonstrated in Fig. 11a, AA exhibited a clear oxidation peak at 0.192 V, with peak

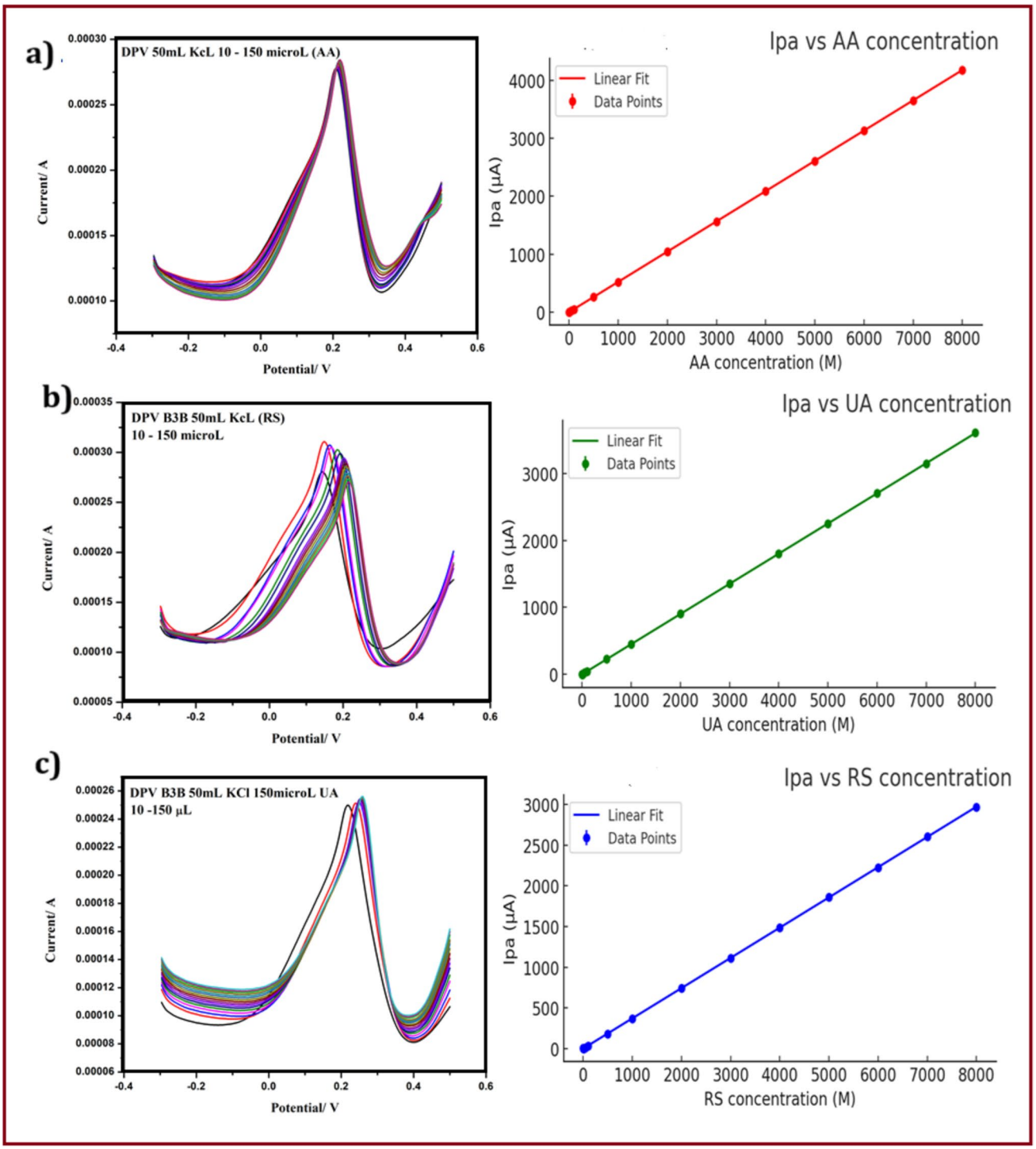

Fig. 11 DPV responses for **a** AA, **b** UA, and **c** RS detection at NSCQD/FeHCF-modified PIGE in 0.1 M KCl (pH 7.0) over a potential window of − 4.0 V to + 4.0 V, with a pulse width of 50 ms, a pulse height of 50 mV, and a step time of 0.5 s

current increasing linearly with concentration. The low oxidation potential and increased peak current indicated the electrode's great sensitivity and catalytic activity for AA oxidation. Similarly, the DPV study of UA revealed a well-defined oxidation peak at 0.352 V, as illustrated in Fig. 11b, with the peak current increasing linearly with UA concentration. This demonstrated the electrode's efficacy in detecting UA with low oxidation potential and great dependability. For RS, the DPV profile revealed an oxidation peak at 0.457 V, as shown in Fig. 11c, with peak current increasing linearly with concentration. Although the peak current for RS was smaller than for AA and UA, the linear trend demonstrated that the electrode was capable of detecting RS with high sensitivity [47]. Strong electrochemical activity was indicated by the DPV response, which showed comparatively high peak currents at low concentrations (10×10^{-6} mol/L). Additional DPV studies were carried out at lower concentrations (0.5×10^{-6} mol/L) in order to further refine the sensor's detection limit. The linear fit curve that resulted from these experiments has been included in Fig. 11a–c. A more accurate assessment of the sensor's sensitivity in ultra-low concentration detection is made possible by the wider concentration range. These findings demonstrated the NSCQD/FeHCF-modified PIGE's capacity to detect each analyte effectively and selectively, indicating increased electrocatalytic activity and appropriateness for multi-analyte electrochemical sensing. The linear correlations between peak current and analyte concentration were further investigated, and regression equations were developed for AA, UA, and RS [48]. The regression equation for AA was found to be Ipa (AA) = 0.5234([AA]/μM) − 3.1245 ($R^2 = 0.9963$), suggesting great sensitivity and precision with a high correlation coefficient. The regression equation for UA detection is Ipa (UA) = 0.4512([UA]/μM) − 2.6743 ($R^2 = 0.9958$), indicating the electrode's high sensitivity and reliability. The regression equation for RS was Ipa (RS) = 0.3721([RS]/μM) − 1.9864 ($R^2 = 0.9967$), indicating a dependable response with slightly lower sensitivity than AA and UA. The linear responses of the NSCQD/FeHCF-modified PIGE were validated by strong correlation coefficients ($R^2 > 0.99$) for all three analytes, demonstrating its precision and reproducibility. The electrode's capacity to detect trace levels was proved by its broader detection ranges and low limits of detection for AA (~2 μM × 10^{-6} mol/L), UA (~3×10^{-6} mol/L), and RS (~5×10^{-6} mol/L). These findings emphasized the modified electrode's adaptability and efficiency for multi-analyte electrochemical sensing, bolstering its potential for use in clinical diagnostics and environmental monitoring.

Practical and real-world setting analysis

CV was used to test the NSCQD/FeHCF-modified PIGE in real-world applications, with Limcee (Vitamin C tablet) for AA detection, Allopurinol tablets for UA, and a hair pigment block solution for RS. Sample concentrations ranged from 5×10^{-6} mol/L to 5000×10^{-6} mol/L, suitable for high-concentration and trace-level detection applications. To establish consistency and eliminate any interferences, the samples were dissolved, sonicated, and filtered. Each Limcee tablet contains 500 mg of Vitamin C, which was dissolved in 100 mL of deionized water and serially diluted to the desired quantities. Each Allopurinol tablet contains 300 mg of UA, which was ground into dispersed in deionized water, sonicated for 15 min, and then filtered before dilution. The hair color block solution was diluted tenfold with ethanol, then further diluted with deionized water to get the RS concentration into the electrochemically detectable range. The results shown in Fig. 12a, b reveal separate oxidation peaks for AA at 0.192 V, UA at 0.352 V, and RS at 0.457 V, with peak currents increasing linearly with analyte concentration, validating the modified electrode's high sensitivity and accuracy even in complex matrices. Consistent oxidation potentials, linear responses, and high peak currents across all three analytes show that the NSC/FeHCF-modified PIGE has higher selectivity and sensitivity. Furthermore, the electrode demonstrated little interference from coexisting compounds, strong repeatability, and good stability, demonstrating its suitability for pharmaceutical, biomedical, and cosmetic industry applications. Recovery percentages validated the sensor's accuracy, ranging from 97.2 to 102.5% for AA, 96.8 to 101.4% for UA, and 95.6 to 103.1% for RS. These findings demonstrate the flexibility and dependability of the NSC/Gr/FeHCF-modified PIGE in real-world electrochemical sensing applications.

Surface area and kinetic analysis

The electroactive surface area of the NSCQD/FeHCF-modified PIGE was estimated using the Randles–Sevcik equation:

$$Ip = (2.69\times10^{5})n^{3/2}AD^{1/2}Cv^{1/2}$$

where Ip is the peak current (A), n is the number of electrons transferred, A is the electroactive surface area (cm^2), D is the diffusion coefficient of the analyte (~7.6×10^{-6} cm^2/s for $Fe(CN)_6^{3-}/Fe(CN)_6^{4-}$), C is the analyte concentration (mol/cm^3), and v is the scan rate (V/s). The modified electrode's surface area was estimated to be approximately 0.23 cm^2, which is considerably greater than that of the bare PIGE (~0.05 cm^2), as determined by experimental CV data. This increase in the electroactive surface area serves as a confirmation of the composite's improved electrocatalytic activity and charge transfer. Moreover, Tafel slope analysis was employed to analyze the kinetics of the electrode reaction from CV data. The logarithmic plot of the anodic peak current vs. potential revealed a Tafel slope of approximately

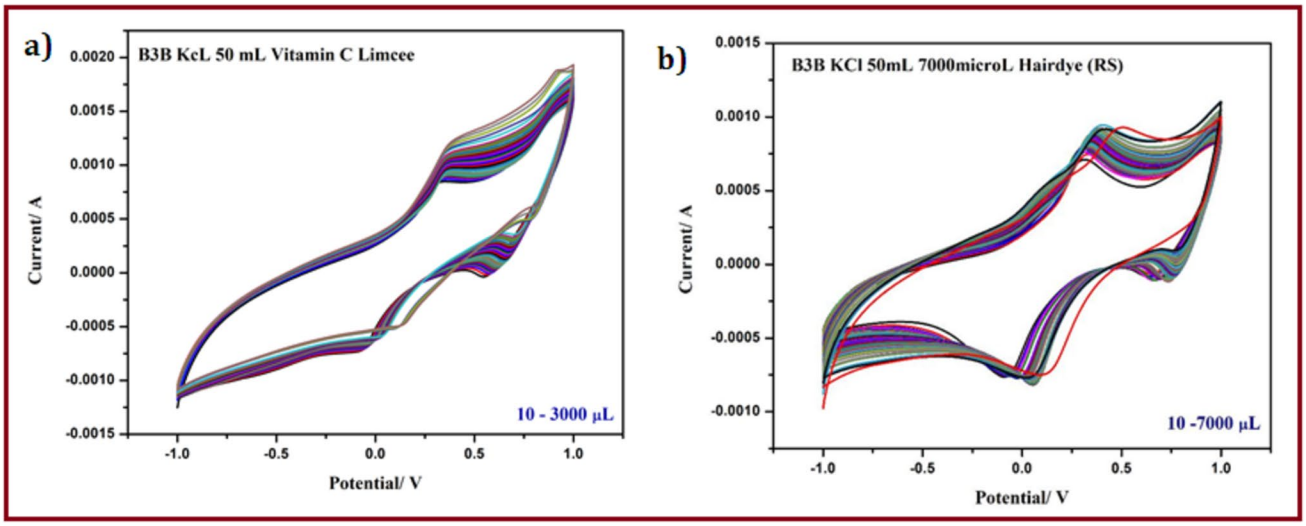

Fig. 12 CV profiles of the NSCQD/Gr/FeHCF-modified PIGE tested for real-world applications: **a** detection of AA in Limcee and **b** detection of RS in hair dye block solution

90–110 mV/dec, suggesting a rapid charge transfer process (Fig. 13a). In addition, the iR decrease observed in CV measurements was used to estimate the solution resistance (Rs) of the PIGE, which was determined to be approximately 12 Ω. The modification predominantly improves charge transfer kinetics, as evidenced by the stable Rs value, rather than increasing solution resistance.

Selectivity and interference study

Electrochemical responses in the presence of possibly interfering compounds were recorded in the NSCQD/FeHCF-modified PIGE under constant primary analyte concentration in order to assess the selectivity of this modification. The influence of dopamine (DA), glucose (Glu), Na^+, K^+, Cl^-, NO_6^-, and SO_4^{2-} on the electrochemical detection of AA, UA, and RS was investigated in this work. Figure 13b shows the results of the interference study in which an equimolar or tenfold excess concentration of interfering species (e.g., 1 mM DA, Glu, Na^+, and K^+) evaluated the current response of 100×10^{-6} of AA, UA, and RS. Glucose and inorganic ions revealed no appreciable interference (< 3% signal deviation), therefore verifying the stability of the sensor in physiological and environmental settings. However, DA exhibited a noticeable interference effect on UA detection (~7.7% response deviation) due to overlapping oxidation potentials. To quantify the relative interference effects, the response deviation was calculated as follows:

$$\%\ of\ Deviation = \left(\frac{I_{withoutinterferent} - I_{with\ interferent}}{I_{without\ interferent}}\right) \times 100\%$$

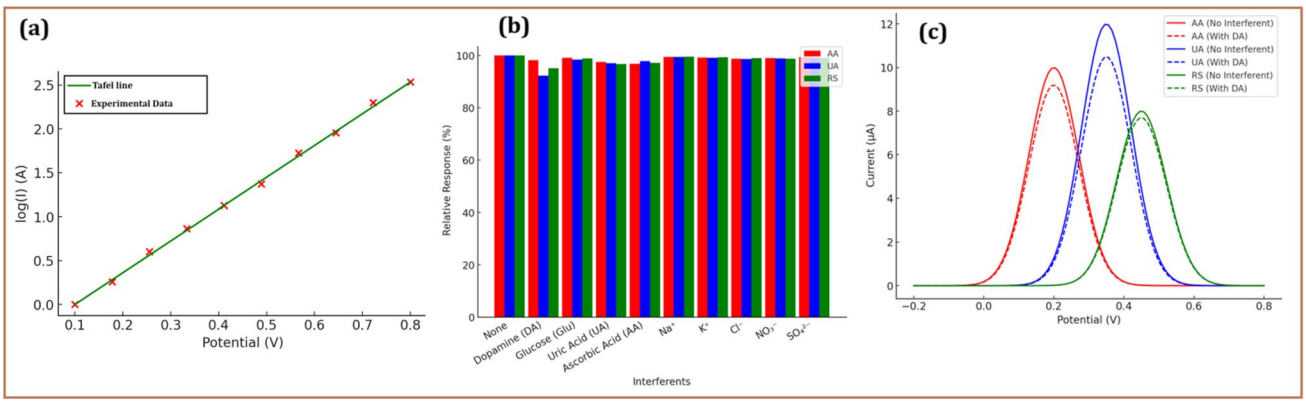

Fig. 13 **a** The logarithmic plot of the anodic peak current vs. potential. **b** Interference study results showing the sensor response to 100 µM AA, UA, and RS in the presence of potential interferents (DA, Glu, Na^+, K^+, Cl^-, NO_3^-, SO_4^{2-}). **c** DPV response of NSCQD/FeHCF-modified PIGE in the presence of potential interferents

The interference effects were determined to be AA (1.8%), UA (7.7%), and RS (4.9%), with dopamine generating the greatest variation in UA detection. To further study the interference effect, DPV studies were performed in the presence and absence of DA, which caused the largest interference in UA detection. Figure 13c depicts the DPV responses of AA, UA, and RS, both with and without DA. The results reveal that the oxidation peak of UA at 0.35 V showed a modest shift and peak suppression (~7.7%) when DA was added, demonstrating mild interference. However, the AA (0.2 V) and RS (0.45 V) peaks were largely unaffected, confirming the sensor's strong selectivity for these analytes in the presence of DA.

Stability, reusability, and comparative analysis with existing electrodes

The NSC/FeHCF-modified PIGE's stability and reusability were assessed through repeated CV and DPV analyses over a period of 50 cycles. The electrode's long-term stability was demonstrated by its capacity to retain more than 95% of its initial current response. Additionally, the electrode's consistent performance and the robustness of the fabrication process were demonstrated by the relative standard deviation (RSD) of less than 3% in reproducibility experiments conducted with three independently fabricated electrodes. These results confirm the electrode's suitability for practical applications that necessitate long-term use. Additionally, the NSC/FeHCF-modified PIGE was evaluated in comparison to electrodes that had been previously reported for the detection of AA, UA, and RS (Table 1) [49–58]. The modified PIGE exhibited substantially reduced oxidation potentials for AA (0.192 V), UA (0.352 V), and RS (0.457 V), in contrast to conventional electrodes. This underscores its improved catalytic activity. Confirming the synergistic effects of its composite structure, these values are significantly lower than those observed in unmodified PIGE or other state-of-the-art electrodes. Furthermore, the modified electrode proved superior at detecting several analytes across a range of sample matrices due to its increased sensitivity and wider detection range.

Mechanism of enhanced electrocatalytic activity in NSC/FeHCF-modified PIGE

The synergistic interaction between the composite components of the NSC/FeHCF-modified PIGE facilitates efficient charge transfer, analyte adsorption, and redox reactions, which is the reason for the enhanced electrocatalytic activity. The graphene (Gr) matrix functions as a highly conductive substrate, reducing the resistance to electron transfer and providing a plentiful number of active sites for analyte adsorption as a result of its extensive surface area [59]. The FeHCF component introduces numerous redox-active centers, including Fe(II)/Fe(III) and C≡N bonds, which directly participate in electron transfer processes. This directly enhances the catalytic efficiency for analyte detection and reduces the oxidation potential. Furthermore, the electrode's performance is further enhanced by the nitrogen and sulfur functionalities in the nitrogen-sulfur-doped carbon (NSC), which generate electron-rich regions that increase the density of active sites and improve analyte adsorption [60]. Electron density and catalytic activity are enhanced by nitrogen dopants, such as pyridine and graphitic N, while

Table 1 Comparison results of present work with previously published work towards AA, UA, and RS detection applications

Sensor material	Analyte	Detection limit	Sensitivity	Linear range	Reference
NiHCF/graphene	AA	0.29 µM	7.029 µA μM^{-1}	0.1–125 µM	[49]
Nickel hexacyanoferrate/poly(1,5-diaminonaphthalene)	AA, UA	0.034 and 0.037 µM	50.31 µA μM^{-1}	600–1000 µM and 600–1000 µM	[50]
NiHCF composite	UA	20 µM	3.3×10^{-7} M	1.0×10^{-6} M to 2.6×10^{-3} M	[51]
Ni-CoHCF/graphene	AA	2.2 nM	-	0.5 to 200	[52]
Graphene/cobalt hexacyanoferrate	RS	-	3.5×10^{-7} mol/L	1.0×10^{-6}–2.0×10^{-6}	[53]
Cd–glutathione	RS	0.2 µM	-	1–14 µM	[54]
NiHCF/MWCNT	UA	50 nM	-	0.1 to 18 µM	[55]
YrHCF/graphene	AA	20 µM	43.3 µA μM^{-1} cm^{-2}	0.5–1.5 µM	[56]
Prussian blue/poly(4-aminosalicylic acid)/uricase	UA	3.0 µM	-	10 to 200 µM	[57]
Cobalt-iron selenides	RS	1.3 µM	2.1×10^{-6} mol/L	5–350 µM	[58]
NSCQD-graphene/iron hexacyanoferrate	AA, UA, RS	2 µM, 3 µM, and 5 µM	0.5234 µA/µM for AA, 0.4512 µA/µM for UA, and 0.3721 µA/µM	10 µM to 8000	This work

S dopants facilitate interactions with analytes, particularly through their functional groups [61]. The oxidation potential is significantly reduced, peak currents are enhanced, and charge transfer kinetics are improved as a consequence of the synergistic integration of Gr, FeHCF, and NSC functionalities. The FeHCF redox-active centers, which catalyze electron transfer, enable oxidation at lower potentials (0.192 V for AA, 0.352 V for UA, and 0.457 V for RS) for AA, UA, and RS. The mechanism entails the diffusion of analytes to the electrode surface, adsorption onto the NSCQD/Gr/FeHCF active sites, electron transfer facilitated by FeHCF, and the subsequent desorption of oxidized products [62, 63]. This integration of components guarantees the electrode's high adaptability, selectivity, and sensitivity for multi-analyte electrochemical sensing.

Conclusions

This study effectively created an NSC/FeHCF-modified PIGE with excellent electrochemical performance for the simultaneous detection of AA, UA, and RS. The sensor was highly sensitive, measuring 523.4 mA/mol/L for AA, 0451.2 mA/mol/L for UA, and 372.1 mA/mol/L for RS. It also had low detection limits of 2×10^{-6} mol/L, 3×10^{-6} mol/L, and 5×10^{-6} mol/L, respectively. The device has a wide linear detection range of 10×10^{-6} mol/L to 8000×10^{-6} mol/L for all three analytes, making it suitable for trace-level quantification and high-concentration applications. Excellent reproducibility was confirmed by stability testing, which showed that the electrode was stable and retained 95% of its initial current response after 50 cycles with a relative standard deviation (RSD) of less than 3%. Using real-world sample analysis, the electrode was further verified by detecting AA in Limcee tablets, UA in Allopurinol tablets, and RS in hair dye solutions with recovery rates higher than 95%. Faster electron transfer, better analyte adsorption, and effective redox reactions were made possible by the synergistic integration of graphene, FeHCF, and NSCQDs, hence enhancing the electrocatalytic activity of the electrode. This resulted in a viable solution for use in clinical, pharmaceutical, and environmental settings. Expanding its application in biological fluids and incorporating it into portable devices for real-time monitoring are the goals of future research.

Acknowledgements The authors express their deep gratitude to the Central Instrumentation Laboratory at Vels University (VISTAS) for their comprehensive support throughout this research. Special thanks are extended to Sathyabama University, Chennai, for providing SEM, XPS characterization, SRM University, Kattankulathur for TEM characterization. We are particularly thankful to Dr. B. Muthuraaman, Department of Energy, University of Madras, Dr. R. Indrajit, Department of Physics, B.S. Abdur Rahman Crescent Institute of Science and Technology, Chennai, and Dr. Gnanam, Department of Physics, Vels Institute of Science and Technology, Chennai, for their invaluable guidance and persistent support in conducting this research.

Author contribution D.S.N. performed conceptualization, experimental design, methodology, formal analysis and writing—original draft. S.D. performed review and editing apart from day-to-day involvement in the progress of the research work. Dr. M. D. contributed to discussion pertained to material selection. R.A.K. coordinating the research activity, including planning and data validation, supervision, project administration and funding acquisition. All authors reviewed the results and approved the final version of the manuscript.

Data availability No datasets were generated or analysed during the current study.

Declarations

Competing interests The authors declare no competing interests.

References

1. Pappenberger G, Hohmann HP (2013) Industrial production of L-ascorbic Acid (Vitamin C) and D-isoascorbic acid. In: Zorn H, Czermak P (eds) Biotechnology of food and feed additives. Advances in Biochemical Engineering/Biotechnology, Vol 143. Springer, Berlin, Heidelberg, pp 143–188
2. Cheng H, Li L, Zhang M, Jiang Y, Yu P, Ma F, Mao L (2018) Recent advances on in vivo analysis of ascorbic acid in brain functions. TrAC, Trends Anal Chem 109:247–259
3. Maiuolo J, Oppedisano F, Gratteri S, Muscoli C, Mollace V (2016) Regulation of uric acid metabolism and excretion. Int J Cardiol 213:8–14
4. Sun HL, Wu YW, Bian HG, Yang H, Wang H, Meng XM, Jin J (2021) Function of uric acid transporters and their inhibitors in hyperuricaemia. Front Pharmacol 12:667753
5. Hahn S (2006) Resorcinol (Vol. No. 71). World Health Organization
6. Gioia C, Banella MB, Vannini M, Celli A, Colonna M, Caretti D (2015) Resorcinol: a potentially bio-based building block for the preparation of sustainable polyesters. Eur Polymer J 73:38–49
7. Li DX, Gan L, Bronja A, Schmitz OJ (2015) Gas chromatography coupled to atmospheric pressure ionization mass spectrometry (GC-API-MS). Anal Chim Acta 891:43–61
8. Pisoschi AM, Pop A, Serban AI, Fafaneata C (2014) Electrochemical methods for ascorbic acid determination. Electrochim Acta 121:443–460
9. Lv J, Li C, Feng S, Chen SM, Ding Y, Chen C., ... Lei W (2019) A novel electrochemical sensor for uric acid detection based on PCN/MWCNT. Ionics 25:4437–4445
10. Zhang M, Li Y, Ma F, Niu Y, Chen X, Ye BC (2023) Metal-organic-framework-derived Ni3ZnC0. 7 materials for highly sensitive electrochemical detection of catechol. Inorg Chem Commun 149:110419
11. Zhu C, Yang G, Li H, Du D, Lin Y (2015) Electrochemical sensors and biosensors based on nanomaterials and nanostructures. Anal Chem 87(1):230–249
12. Prabakar SR, Narayanan SS (2007) Amperometric determination of paracetomol by a surface modified cobalt hexacyanoferrate graphite wax composite electrode. Talanta 72(5):1818–1827
13. Narayanan SS, Scholz F (1999) A comparative study of the electrocatalytic activities of some metal hexacyanoferrates for the oxidation of hydrazine. Electroanalysis: Int J Devoted Fundam Pract Asp Electroanal 11(7):465–469

14. Prabakar SR, Narayanan SS (2009) Catalytic oxidation of dopamine at a nickel hexacyanoferrate surface modified graphite wax composite electrode coated with Nafion. Electroanalysis: Int J Devoted Fundam Pract Asp Electroanal 21(13):1481–1489
15. Ghica ME, Carvalho RC, Amine A, Brett CM (2013) Glucose oxidase enzyme inhibition sensors for heavy metals at carbon film electrodes modified with cobalt or copper hexacyanoferrate. Sens Actuators, B Chem 178:270–278
16. Rani M, Shanker U, Sillanpää M (2024) Green synthesized metal hexacyanoferrate based nanostructures for environmental applications. Inorg Chem Commun 161:112058
17. Rajpurohit AS, Srivastava AK (2019) Simultaneous electrochemical sensing of three prevalent anti-allergic drugs utilizing nanostructured manganese hexacyanoferrate/chitosan modified screen printed electrode. Sens Actuators, B Chem 294:231–244
18. García T, Casero E, Lorenzo E, Pariente F (2005) Electrochemical sensor for sulfite determination based on iron hexacyanoferrate film modified electrodes. Sens Actuators, B Chem 106(2):803–809
19. Shanker U, Jassal V, Rani M (2017) Green synthesis of iron hexacyanoferrate nanoparticles: potential candidate for the degradation of toxic PAHs. J Environ Chem Eng 5(4):4108–4120
20. Xu D, Lin Q, Chang HT (2020) Recent advances and sensing applications of carbon dots. Small Methods 4(4):1900387
21. Liu ML, Chen BB, Li CM, Huang CZ (2019) Carbon dots: synthesis, formation mechanism, fluorescence origin and sensing applications. Green Chem 21(3):449–471
22. Ji C, Zhou Y, Leblanc RM, Peng Z (2020) Recent developments of carbon dots in biosensing: a review. ACS sensors 5(9):2724–2741
23. Ding H, Wei JS, Xiong HM (2014) Nitrogen and sulfur co-doped carbon dots with strong blue luminescence. Nanoscale 6(22):13817–13823
24. Wang Y, Kim SH, Feng L (2015) Highly luminescent N, S-Co-doped carbon dots and their direct use as mercury (II) sensor. Anal Chim Acta 890:134–142
25. Zhao P, Li X, Baryshnikov G, Wu B, Ågren H, Zhang J, Zhu L (2018) One-step solvothermal synthesis of high-emissive amphiphilic carbon dots via rigidity derivation. Chem Sci 9(5):1323–1329
26. Han Z, He L, Pan S, Liu H, Hu X (2020) Hydrothermal synthesis of carbon dots and their application for detection of chlorogenic acid. Luminescence 35(7):989–997
27. Wang Q, Zheng H, Long Y, Zhang L, Gao M, Bai W (2011) Microwave–hydrothermal synthesis of fluorescent carbon dots from graphite oxide. Carbon 49(9):3134–3140
28. Tang W, Wang B, Li J, Li Y, Zhang Y, Quan H, Huang Z (2019) Facile pyrolysis synthesis of ionic liquid capped carbon dots and subsequent application as the water-based lubricant additives. J Mater Sci 54:1171–1183
29. Wang S, Morelos-Gómez A, Lei Z, Terrones M, Takeuchi K, Sugimoto W, Endo M, Kaneko K (2016) Correlation in structure and properties of highly-porous graphene monoliths studied with a thermal treatment method. Carbon 96:174–183
30. Zou G, Zhang D, Dong C, Li H, Xiong K, Fei L, Qian Y (2006) Carbon nanofibers: synthesis, characterization, and electrochemical properties. Carbon 44(5):828–832
31. Wang H, Bian Y, Hu J, Dai L (2018) Highly crystalline sulfur-doped carbon nitride as photocatalyst for efficient visible-light hydrogen generation. Appl Catal B 238:592–598
32. Lan H, Wang J, Cheng L, Yu D, Wang H, Guo L (2024) The synthesis and application of crystalline–amorphous hybrid materials. Chem Soc Rev 53(2):684–713
33. Gutiérrez-Becerra A, Martínez-Martínez F, Bárcena-Soto M, Casillas N, Ceja I, Prévost S, Gradzielski M, Escalante JI (2014) Direct synthesis of different metal hexacyanoferrate nanoparticles in reverse microemulsions by using a ferrocyanide functionalized surfactant. Colloids and Surfaces A: Physicochemical and Engineering Aspects 444:63–68
34. Arunprasad V, Siva Karthik P, Thulasi S, Arul GP, Mohd Shkir, Rajamanickam AT, Sumathi T, Fredrick SR (2022) Hydrothermal preparation of Ni3S4/CoS2 composite electrocatalytic materials for high performance counter electrodes of dye-sensitized solar cells. J Clust Sci 33:2651–2659
35. Ghosh T, Nandi S, Bhattacharyya SK, Ghosh SK, Mandal M, Banerji P, Das NC (2023) Nitrogen and sulphur doped carbon dot: an excellent biocompatible candidate for in-vitro cancer cell imaging and beyond. Environ Res 217:114922
36. Fan Z, Wang W, Ren J, Zhang S, Ren R, Lv YK (2024) Additive-free, in situ rapid repair of vacancies in Fe [Fe (CN) 6] electrodes for efficient capacitive deionization. Langmuir 40(39):20725–20735
37. Yuan H, Meng Y, Li B, Zhu F (2025) Innovative three-layered FeHCF@ MnHCF@ FeHCF core-shell design for enhanced sodium-ion battery cathode performance. J Energy Storage 110:115307
38. Cataldi TR, Guascito R, Salvi AM (1996) XPS study and electrochemical behaviour of the nickel hexacyanoferrate film electrode upon treatment in alkaline solutions. J Electroanal Chem 417(1–2):83–88
39. Fang S, Xia Y, Lv K, Li Q, Sun J, Li M (2016) Effect of carbon-dots modification on the structure and photocatalytic activity of g-C3N4. Appl Catal B 185:225–232
40. Yang Y, Hao Y, Niu L, Xia F (2015) In situ co-deposition of nickel hexacyanoferrate nanocubes on the reduced graphene oxides for supercapacitors. Carbon 84:174–184
41. Ananthappan P, Thangarasu M, Vasantha VS (2024) Effect of electrophoretic deposition for selective detection of Pb2+ ions using nitrogen and sulphur-doped reduced graphene oxide. Microchem J 203:110879
42. Jiang WJ, Tang T, Zhang Y, Hu JS (2020) Synergistic modulation of non-precious-metal electrocatalysts for advanced water splitting. Acc Chem Res 53(6):1111–1123
43. Wang L, Zhen M, Hu Z (2023) Status and prospects of electrocatalysts for lithium-sulfur battery under lean electrolyte and high sulfur loading conditions. Chem Eng J 452:139344
44. Manikandan VS, Adhikari B, Chen A (2018) Nanomaterial based electrochemical sensors for the safety and quality control of food and beverages. Analyst 143(19):4537–4554
45. Júnior JGMC, Ferreira GMM, de Oliveira FG, Damos FS, Luz RDCS (2014) A novel platform based on graphene/poly (3, 4-ethylenedioxythiophene)/iron (III) hexacyanoferrate (II) composite film for electrocatalytic reduction of H_2O_2. J Electroanal Chem 732:93–100
46. Hassan R, Ibrahim S (2019) Reduction of tellurium (IV) by ascorbic acid in acid perchlorate solutions. A kinetic and mechanistics approach on the nature of electron-transfer process. Inorg Chem Commun 104:178–185
47. Lv M, Wang X, Li J, Yang X, Zhang CA, Yang J, Hu H (2013) Cyclodextrin-reduced graphene oxide hybrid nanosheets for the simultaneous determination of lead (II) and cadmium (II) using square wave anodic stripping voltammetry. Electrochim Acta 108:412–420
48. Atta NF, El-Kady MF, Galal A (2010) Simultaneous determination of catecholamines, uric acid and ascorbic acid at physiological levels using poly (N-methylpyrrole)/Pd-nanoclusters sensor. Anal Biochem 400(1):78–88
49. Banavath R, Abhinav A, Srivastava R, Bhargava P (2022) Highly sensitive ascorbic acid sensors from EDTA chelation derived nickel hexacyanoferrate/graphene nanocomposites. Electrochim Acta 419:140335
50. Hathoot AA, Hassan KM, Essa WA, Abdel-Azzem M (2017) Simultaneous determination of ascorbic acid, uric acid and

dopamine at modified electrode based on hybrid nickel hexacyanoferrate/poly (1, 5-diaminonaphthalene). J Iran Chem Soc 14:1789–1799
51. Babu RS, Prabhu P, Narayanan SS (2011) Selective electrooxidation of uric acid in presence of ascorbic acid at a room temperature ionic liquid/nickel hexacyanoferarrate nanoparticles composite electrode. Colloids Surf, B 88(2):755–763
52. Wang Q, Tang Q (2015) Improved sensing of dopamine and ascorbic acid using a glassy carbon electrode modified with electrochemically synthesized nickel-cobalt hexacyanoferrate microparticles deposited on graphene. Microchim Acta 182:671–677
53. Huang K, Yu S, Wang L, Gan T, Li M (2012) Simultaneous determination of hydroquinone, catechol and resorcinol based on graphene/cobalt hexacyanoferrate modified glassy carbon electrode. Acta Chim Sinica 70(06):735
54. Aslam R, Fatima B, Hussain D, Nawaz R, Majeed S, Ashiq MN, Qureshi TI, Najam-Ul-Haq M (2020) Sensitive and high recovery electrochemical sensing of resorcinol by Cd–glutathione complex-modified glassy carbon electrode. Int J Environ Anal Chem 101(15):2785–2795
55. Fang B, Feng Y, Wang G, Zhang C, Gu A, Liu M (2011) A uric acid sensor based on electrodeposition of nickel hexacyanoferrate nanoparticles on an electrode modified with multi-walled carbon nanotubes. Microchim Acta 173:27–32
56. Hatamie A, Rahmati R, Rezvani E, Angizi S, Simchi A (2019) Yttrium hexacyanoferrate microflowers on freestanding three-dimensional graphene substrates for ascorbic acid detection. ACS Appl Nano Mater 2(4):2212–2221
57. da Cruz FS, de Souza Paula F, Franco DL, dos Santos WTP, Ferreira LF (2017) Electrochemical detection of uric acid using graphite screen-printed electrodes modified with Prussian blue/poly (4-aminosalicylic acid)/Uricase. J Electroanal Chem 806:172–179
58. Yin D, Liu J, Bo X, Guo L (2020) Cobalt-iron selenides embedded in porous carbon nanofibers for simultaneous electrochemical detection of trace of hydroquinone, catechol and resorcinol. Anal Chim Acta 1093:35–42
59. Gan T, Hu S (2011) Electrochemical sensors based on graphene materials. Microchim Acta 175:1–19
60. Zhang R, Zhang C, Zheng F, Li X, Sun CL, Chen W (2018) Nitrogen and sulfur co-doped graphene nanoribbons: a novel metal-free catalyst for high performance electrochemical detection of 2, 4, 6-trinitrotoluene (TNT). Carbon 126:328–337
61. Perazzolo V, Grądzka E, Durante C, Pilot R, Vicentini N, Rizzi GA, Granozzi G, Gennaro A (2016) Chemical and electrochemical stability of nitrogen and sulphur doped mesoporous carbons. Electrochimic Acta 197:251–262
62. Ulgut B, Abruna HD (2008) Electron transfer through molecules and assemblies at electrode surfaces. Chem Rev 108(7):2721–2736
63. Zhen Q, Ma H, Jin Z, Zhu D, Liu X, Sun Y, Zhang C, Pang H (2021) Electrochemical sensor for rutin detection based on N-doped mesoporous carbon nanospheres and graphene. New J Chem 45(11):4986–4993